ACS APPLIED NANO MATERIALS
Cite This: ACS Appl. Nano Mater. 2019, 2, 228−240
Article
www.acsanm.org

Thermal Modification of Graphite for Fast Electron Transport and Increased Capacitance

O. Charles Nwamba,[†] Elena Echeverria,[‡] David N. McIlroy,[‡] Aaron Austin,[‡] Jean'ne M. Shreeve,[†] and D. Eric Aston*[,§]

[†]Department of Chemistry, University of Idaho, 875 Perimeter Drive MS 2343, Moscow, Idaho 83844-2343, United States
[‡]Department of Physics, Oklahoma State University, 145 Physical Science Bldg., Stillwater, Oklahoma 74078, United States
[§]Department of Chemical and Materials Engineering, University of Idaho, 875 Perimeter Drive MS 1021, Moscow, Idaho 83844-1021, United States

Supporting Information

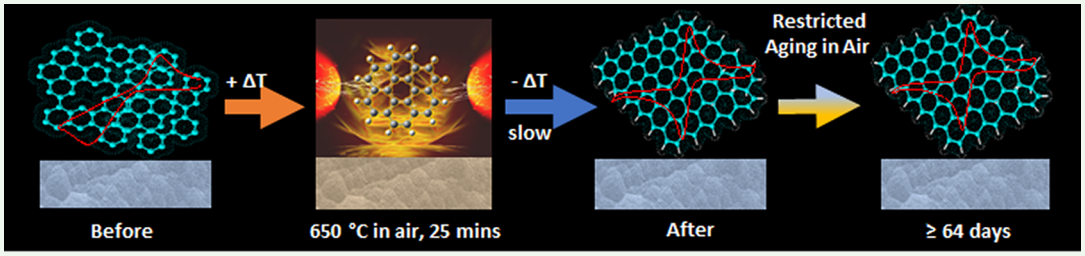

ABSTRACT: On thermal treatment, eight different graphite materials became resistant to air aging for at least 9 weeks compared to the usual time of hours to a few days when assayed in 1 mM ferri-ferrocyanide solution. In addition, resistance to aging lasted at least 7 days when immersed in 1 mM ferri-ferrocyanide solution compared to the frequently reported few minutes to hours. Experimental results confirm that with heat treatment, HOPG-ZYH, graphite rods, pyrolytic graphites, graphite felts, and natural and artificial graphites undergo structural reorganization that leads to restructuring of their electronic nature. This electronic restructuring enhances and sustains their electrochemical properties. The extent of reorganization is dependent on the initial disordered state, which in turn is important to the final structural and electronic conditions. These results strongly suggest that the primary factor enhancing the electronic response of heat-treated materials is from an overall higher density of states (DOS) localized on delocalizing π bonds compared to their controls. This structural reorganization of the graphites also supports a degree of crystallinity along the lattice sites that enables carrier hopping irrespective of adventitious oxygen-containing and hydrocarbon moieties that are associated with aging-induced sluggish electron transfer kinetics. The attributes of this electronic structure demonstrate a strongly correlated system that exhibits a nonperturbative behavior. A one-dimensional Hubbard model describes this behavior to explain the surface-to-electronic chemistry of treated graphites by addressing both their enhanced electrochemical performance and their delayed or reduced aging effects.

KEYWORDS: *graphites, aging, fast HET, disorder, density of states, electronic structure*

INTRODUCTION

Heterogeneous electron transfer (HET) kinetics are fundamental in solid carbon material (electrode)−electrolyte interactions and play significant roles in molecular electronics, electrochemical energy storage and conversion, sensing, and electro-oxidative reactions.[1−10] The electronic density of states (DOS) dominates the HET kinetics of these carbon materials because of the probability that an electron with the appropriate energy may transfer to a redox probe.[11−14] Thus, the HET rate increases when the electrode having sufficient electronic states with energies near the formal potential level of the redox probe involved has overlap between its (electrode) energy levels and those of the redox states in solution.[5,12−16] Electronic states of carbon electrodes could be determined by surface states or structures[11,14,17] such as defects[14,18,19] and functional groups.[14,20] It is thought that the kinetic preferences of these functional groups for electron transport, even though often unknown,[20] remain a key component for the resultant electrochemical responses of carbon materials to redox probes.[20] Thus, techniques and/or procedures aimed at increasing the DOS by either introducing, modulating, and/or manipulating surface functional groups and defects ultimately result in reciprocated responses to electrochemical activities of carbon electrodes. These include mechanical polishing, as commonly employed on glassy carbon electrodes, vacuum heat treatment or heating under inert gas, combined treatment of the electrode with organic solvents and activated carbon, laser ablation or laser-based thermal treatment

Received: October 21, 2018
Accepted: December 6, 2018
Published: December 6, 2018

DOI: 10.1021/acsanm.8b01887
ACS Appl. Nano Mater. 2019, 2, 228−240

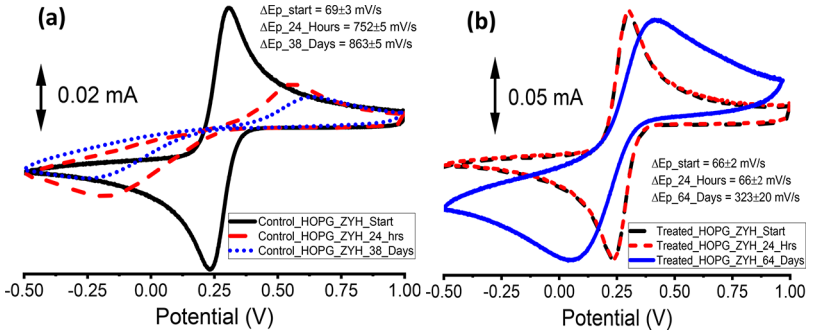

Figure 1. Cyclic voltammogram (CV) trends for the control (a) and treated (b) HOPG-ZYH at the start (black), 24 h (red dashed line), and end of the experiment (ν = 0.05 V/s in 1 mM ferri-ferrocyanide; n = 3): (a) dotted blue CV at 38 days, (b) solid blue CV at 64 days.

Table 1. ΔE_p (mV) and Accompanying Rate Constants[a] of the Treated and Control Graphites Aged in Air

electrode	type	ΔE_p (start) (mV)	$K_{(start)}{}^0$ ($cm^2 \cdot s^{-1}$)	end day	ΔE_p (end) (mV)	$K_{(end)}{}^0$ ($cm^2 \cdot s^{-1}$)
HOPG-ZYH	C	69 ± 3	$1.79 \times 10^{-2} \pm 6.5 \times 10^{-3}$	38	863 ± 5	$6.32 \times 10^{-7} \pm 5.7 \times 10^{-8}$
	T	66 ± 2	$2.61 \times 10^{-2} \pm 1.8 \times 10^{-2}$	64	323 ± 20	$3.40 \times 10^{-4} \pm 2.9 \times 10^{-5}$
PG(K&J)	C	312 ± 48	$3.53 \times 10^{-4} \pm 8.0 \times 10^{-5}$	63	532 ± 56	$1.76 \times 10^{-4} \pm 2.3 \times 10^{-5}$
	T	65 ± 1	$3.26 \times 10^{-2} \pm 2.0 \times 10^{-2}$	64	76 ± 2	$1.09 \times 10^{-2} \pm 1.1 \times 10^{-3}$
PG(UN)	C	183 ± 30	$1.10 \times 10^{-3} \pm 4.0 \times 10^{-4}$	63	430 ± 69	$2.30 \times 10^{-4} \pm 5.0 \times 10^{-5}$
	T	65 ± 2	$3.26 \times 10^{-2} \pm 9.8 \times 10^{-3}$	64	84 ± 2	$6.52 \times 10^{-3} \pm 4.0 \times 10^{-4}$
artificial graphite	C	425 ± 14	$2.33 \times 10^{-4} \pm 9.5 \times 10^{-6}$	63	573 ± 23	$1.19 \times 10^{-4} \pm 5.1 \times 10^{-5}$
	T	66 ± 4	0.026 ± (*) ± (*) = 0.026−0.016 to 0.026 + 0.036	64	93 ± 2	$4.77 \times 10^{-3} \pm 2.9 \times 10^{-4}$
natural graphite	C	74 ± 7	$1.20 \times 10^{-2} \pm 5.0 \times 10^{-3}$	63	105 ± 4	$3.26 \times 10^{-3} \pm 3.8 \times 10^{-4}$
	T	65 ± 2	$3.26 \times 10^{-2} \pm 9.8 \times 10^{-3}$	64	90 ± 4	$5.30 \times 10^{-3} \pm 7.6 \times 10^{-4}$
mech stressed natural graphite	C	145 ± 25	$1.60 \times 10^{-3} \pm 5.0 \times 10^{-4}$	63	245 ± 6	$5.10 \times 10^{-4} \pm 2.0 \times 10^{-5}$
	T	67 ± 2	$2.28 \times 10^{-2} \pm 7.3 \times 10^{-3}$	64	89 ± 8	$5.50 \times 10^{-3} \pm 2.0 \times 10^{-3}$
graphite rod	C	69 ± 2	$1.80 \times 10^{-2} \pm 4.0 \times 10^{-3}$	63	94 ± 8	$4.60 \times 10^{-3} \pm 1.2 \times 10^{-3}$
	T	40 ± 2	1.02 ± 0.09	64	40 ± 2	1.02 ± 0.08
GFA3	C	211 ± 22	$6.50 \times 10^{-4} \pm 2.5 \times 10^{-4}$	82	66 ± 2	$2.61 \times 10^{-2} \pm 9.8 \times 10^{-3}$
	T	171 ± 14	$1.20 \times 10^{-3} \pm 2.0 \times 10^{-4}$	82	118 ± 4	$2.50 \times 10^{-3} \pm 2.0 \times 10^{-4}$
GFA5	C	165 ± 19	$1.30 \times 10^{-3} \pm 3.0 \times 10^{-4}$	85	93 ± 9	$4.76 \times 10^{-3} \pm 1.4 \times 10^{-3}$
	T	150 ± 7	$1.50 \times 10^{-3} \pm 1.0 \times 10^{-4}$	85	128 ± 3	$2.10 \times 10^{-3} \pm 1.0 \times 10^{-4}$

[a] k^0 [cm/s] in 1 mM $Fe[(CN)_6]^{3-/4-}$ and at ν = 0.05 V/s. n = 3.

protocols, electrochemical polarization such as preanodization, various chemical exposures, and plasma activation treatments with radio frequency (RF), hydrogen, and microwave.[21,22]

Treatment procedures aim to improve one or more properties of the graphite and/or carbon materials, such as capacitance[23−26] and/or the HET kinetics property of solid electrodes[27,28] via various mechanisms, though sometimes similar. Regarding electron transport, different treatment procedures yield structurally distinct surfaces with varying electron transfer rate constants.[27] For example, laser ablation and vacuum thermal treatments can promote electron transfer by desorption of impurities and formation[28−30] or exposure of active regions[28,29] without the contribution of oxygen-containing functional groups.[28] Additionally, laser treatment and anodization promote fast electron transfer by creating edge plane defects,[27] while treatment with organic reagents promotes electron transfer by desorbing impurities from electrode surfaces.[31] However, chemisorbed species, particularly oxygen containing groups[28,31−33] and hydrocarbons[34−37] on carbon electrode surfaces such as graphite and graphene, can hamper electron transfer kinetics. Thus, it is generally accepted that the surfaces of solid carbonaceous electrodes are gradually deactivated during exposure, and adsorption of adventitious impurities from air or electrolyte solutions preceding electrochemical experiments[38] result in sluggish heterogeneous electron transfer (HET) kinetics because of aging[22] and accompanying impediments for various uses of carbon materials.[6,11]

The present work focuses on resistance to aging of graphite materials thermally treated in air for at least 9 weeks and in a ferri-ferrocyanide redox couple ($[(Fe(CN)_6]^{3-/4-}$ (1 M KCl)) for 7 days. Results include a total of eight carbon materials including HOPG-ZYH, two different pyrolytic graphites, artificial and natural graphites, graphite rod, and two graphite felts (GFA3 and GFA5). Investigations on material behaviors through FTIR, Raman, XPS, UPS, and water contact angle measurements were designed for periodic monitoring and evaluation of resistance to aging relative to control samples undergoing no heat treatment. Graphite heat treatments typically result in higher-ordered physicochemical states, which can be described via the folding funnel model.[39−41] Empirical data in support of the model implies that there exists a path to a minimum Gibbs free energy of extent of crystallinity—or more probably a multiconfigurational ensemble of localized minima of metastable and stable states in real materials—irrespective of the starting graphite (with respect to the graphites employed herein) such that the converted microscopic graphite state is mainly aromatic. This new

DOI: 10.1021/acsanm.8b01887
ACS Appl. Nano Mater. 2019, 2, 228−240

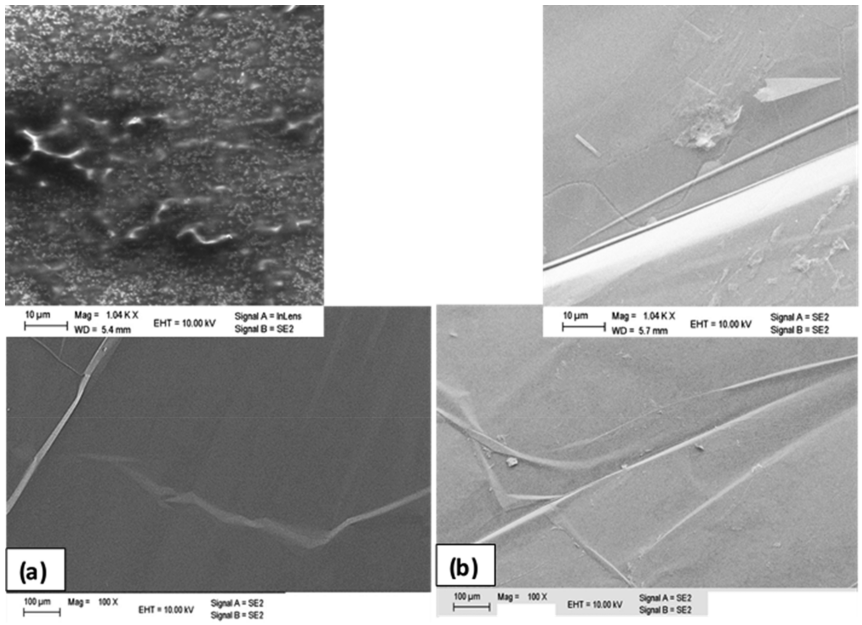

Figure 2. SEM micrographs of (a) the control and (b) treated HOPG-ZYH (scale bars: 100 μm); top images are higher magnifications (1.04k×), scale bars: 10 μm.

graphite state would possess a degree of crystallinity along the lattice sites that enables carrier hopping irrespective of adventitious oxygen-containing and hydrocarbon moieties, which are synonymous with aging-induced sluggish electron transfer kinetics. This would suggest an unperturbed or lesser perturbed electronic structure signifying a diminution of Coulombic (repulsive) contributive forces. A one-dimensional Hubbard model[42] facilitates an explanation of the surface-to-electronic (or vice versa) chemistry of the treated graphite materials where the heat-treated materials have enhanced and sustained electronic/electrochemical properties in contrast to the controls and irrespective of any adventitious functional surface groups.

RESULTS AND DISCUSSION

Cyclic voltammograms (CVs) of control and treated graphite materials in 1 mM $[Fe(CN)_6]^{3-/4-}$ redox couple solution are shown in Figure 1 for the HOPG-ZYH samples as an example comparator, while the other graphitic materials are in the Supporting Information (Figure S1). The ΔE_p of the control graphites widened on subsequent scans signifying increasingly sluggish electron transfer. This is unlike the treated materials that had steady and consistent CVs on scanning several times in the redox solution, since in general, the electron transfer response of carbon electrodes deteriorates on subsequent scans in redox couples.[17,43,44] The ΔE_p of the control HOPG-ZYH was 65 ± 5 mV when peeled fresh. These electrodes aged to 760 ± 5 mV in 24 h and did not age much afterward even at the end of 38 days when testing halted on its control (Table 1). The other control graphites behaved similarly to the HOPG, having much higher ΔE_p at the end of the air-aging experiment. The treated HOPG had a higher than usual ΔE_p at the end of 64 days unlike the other treated graphites.

The CVs of the treated graphites, when compared to their controls and graphite/carbon materials from the literature,[2,12,35,44,45] suggest that surface structural and/or electronic changes are responsible for our observations. Additionally, the increase in HET across eight different graphite materials from various graphitic strata indicates that whatever mechanism is responsible for the trend is common for graphitic materials. In addition to fast HET, the increased capacitance of graphite felts (GFA3 and GFA5 (Figure S1(h1-i2)) and the symmetric behavior of the treated graphite rod capacitance, even at high scan rates (Figure S1(g2)), suggest that thermal treatment modulates not just the pathway for fast HET kinetics alone but probably other electrochemical properties of the graphites (in this case, the graphite felt capacitance). Whichever the mechanism(s) of change involved would have likely modulated the fundamental structure(s) of these materials. These would include, for example, their degree of crystallinity, Raman signatures such as the intensity ratios of their D-to-G bands, and other electronic properties such as their LUMO and HOMO bands. Enhanced HET in aged control graphite felts over the fresh controls without a corresponding increase in capacitance is noteworthy, and its importance is further discussed with the XPS results.

The heterogeneous electron transfer rate constants (k^0 [cm/s]) for the pristine control (denoted with "C") and thermally treated graphites (denoted with "T") in Table 1 derive from the relationship between peak potential separation (ΔE_p [mV]) and the kinetic parameter ψ (see ref 46 for ψ values) according to the Nicholson equation[46]

$$k^0 = \psi\left[D_0\pi\nu\left(\frac{nF}{RT}\right)\right]^{1/2}\left(\frac{D_0}{D_R}\right)^{-(\alpha/2)} \quad (1)$$

The rate constant results apply for α = 0.5, and diffusion coefficient values apply for $Fe(CN)_6^{3-/4-}$ (1 M KCl) of D_O (7.32×10^{-6} cm^2·s^{-1}) and D_R (6.67×10^{-6} cm^2·s^{-1}).[47]

Unlike previous reports where HOPG-ZYH heated at 650 °C formed multilayer pits,[48,49] the treated HOPG-ZYH surface shows no pits and limited flaking with step defects seen also in control samples (Figure 2). Higher magnifications hint at limited surface exfoliation to expose few layers. Control samples show only surface roughness and defects attributable to the typical process of removal from bulk samples. A lack of

DOI: 10.1021/acsanm.8b01887
ACS Appl. Nano Mater. 2019, 2, 228−240

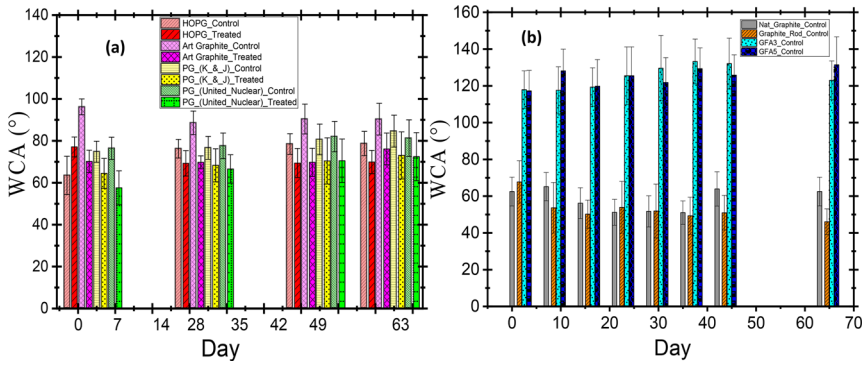

Figure 3. Water contact angles (WCA) with (a) HOPG at the numbered day of test (only 0, 21, 42, and 63 are shown) clustered from left to right with artificial graphite-, PG(K&J)-, and PG(UN)-treated sample data overlaying the control data of mostly higher values. (The entire set for the 9 week study is shown in Figure S3a); (b) natural graphite clustered left to right with graphite rod and felt (GFA3 and GFA5) control samples with all thermally treated samples as totally wetting and not shown (see Videos i, ii, and iii).

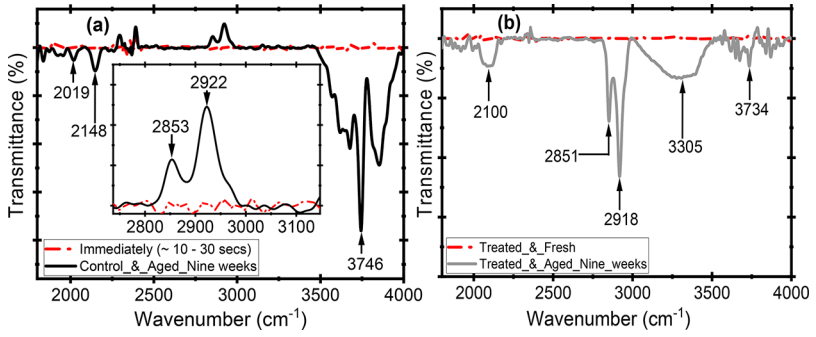

Figure 4. ATR-FTIR spectra of (a) control and (b) treated HOPG-ZYH at the start of experiment (red dash-dot) and at the end of 9 weeks of aging in the lab atmosphere (solid). Inset: magnified region.

pitting on treated samples suggests that the facile electron transport even when aged cannot be mainly attributed to edge exposure.

Other extended and planar graphites when treated show no changes in surface morphology when compared to their controls (Figure S2), although fiber felts GFA3 and GFA5 do (Figure S2). Even though the formation[28−30] or exposure of active regions[28,29] such as step or edge defects on graphite basal planes facilitate HET,[17,45,50−55] the SEM micrographs reveal only slight etching on the graphite felts. This strongly implies that surface defects are not generally responsible for facile HET in the treated graphites, since all sets displayed heat-treatment-induced HET kinetics enhancement.

Graphite felts have disordered or mutually disoriented crystallites with exposed edges on their carbon fibers that are prone to oxidative attack from thermal treatment.[56] However, such edge-density exposure leading to accelerated HET is known to be deactivated quickly,[12,21] even within minutes or hours when exposed in air.[57,58] This is unlike the treated graphites employed in this study that still show very good HET kinetics even at the end of, at least, 64 days in air. The PG aged in 1 mM ferri-ferrocyanide increased in ΔE_p by about 40 mV in 7 days (Figure S2), unlike reported increases in ΔE_p of several hundreds of mV over a few hours.[59]

Water contact angles (WCA) of both control and treated graphite groups over the course of aging show that thermal treatment increases wettability (Figure 3), even from fully hydrophobic (Figure 3b) to completely wet out (0° not shown) in the cases of porous graphites (see Videos i, ii, and iii for the dynamic contact angles of treated graphite felts, natural graphite, and graphite rod, respectively). WCA correlates with surface chemistry and roughness as well as heterogeneity or patterns thereof.[60,61] WCA values near 60° for treated samples are consistent with the definition of hydrophilicity for graphite and its graphene derivatives. Those of the controls (WCA ≥ 80°) are also consistent with hydrophobicities of graphites and graphenes.[62,63] Artificial graphite show hydrophobic WCAs ≥ 90° unlike the HOPG-ZYH and PGs of roughly 80°. Lower WCA values in controls are attributed to native edge densities on their basal planes, which reportedly lowers the WCA in otherwise hydrophobic graphitic materials.[64] Also of note is the wetting of control graphite felts (GFA3 and 5) from the 35th day and onward (see Video iv) even though individual fibers still exhibit clear hydrophobicity, for example, in residual water beading at apparent angles approaching 180° indicating extreme surface chemical heterogeneities (Figure S3 and Videos iv and v). The WCA results suggest that it is likely that surface functional group differences between the control and treated materials could be responsible for the differences in wetting behavior.[65−67]

ATR-FTIR spectra of aged samples for both control and treated HOPG show peaks near 2100 cm^{-1} associated with silanol polymers, ~3740 cm^{-1} associated with reactive Si−OH, and 3350 cm^{-1} arising from normal polymeric OH stretches[68] compared to fresh samples (Figure 4). The Si-related modes derive from contaminants of exposure to airborne soil particles.[69] Prominent peaks at ~2850 and 2920−2930 cm^{-1} also arise in aged (control and treated) samples, being modes from symmetric and asymmetric methylene vibrations, respectively, widely expected to cause high WCA values of

DOI: 10.1021/acsanm.8b01887
ACS Appl. Nano Mater. 2019, 2, 228−240

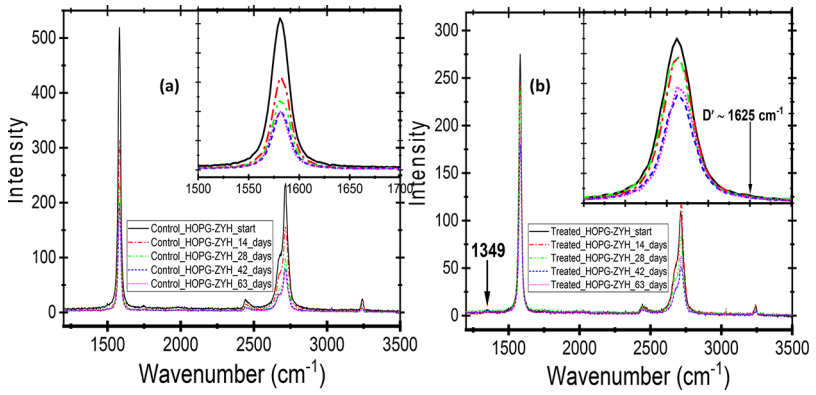

Figure 5. Raman spectra of (a) control and (b) treated HOPG-ZYH. Insets: Graphite (G) bands magnified. The treated HOPG now has a small bump near 1350 cm^{-1} synonymous with the disorder-induced D band and another disorder-induced band near 1625 cm^{-1}, the D′ band.

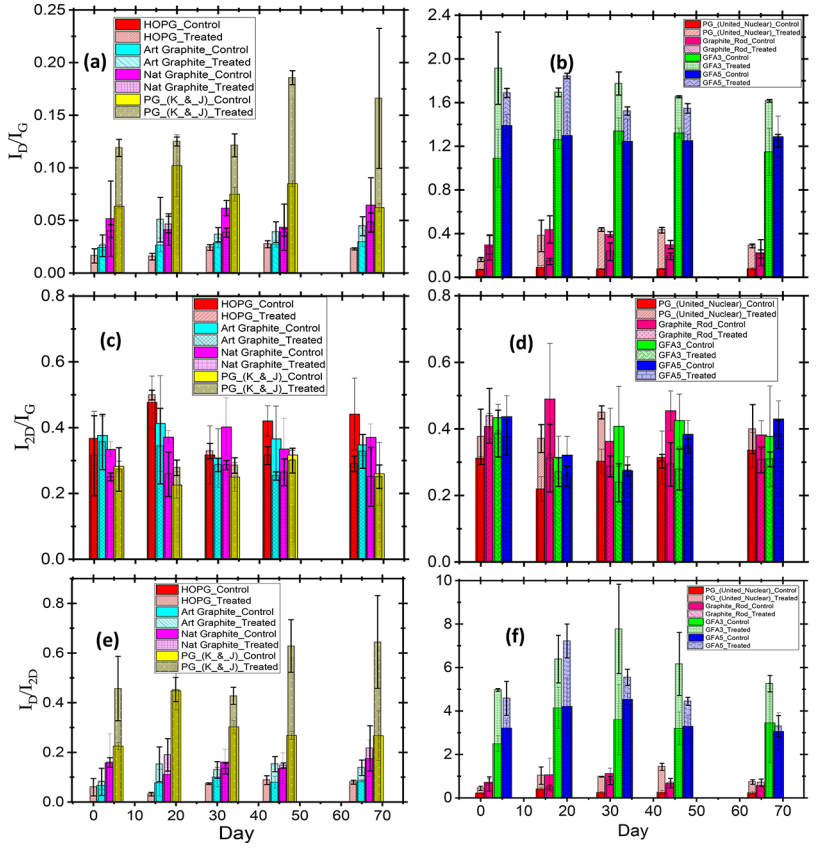

Figure 6. Raman-band peak intensity ratios vs days of aging in air (n = 4 per sample type): (a,b) D-to-G band (I_D/I_G) indicating degree of disorder; (c,d) 2D-to-G band (I_{2D}/I_G) and (e,f) D-to-2D (I_D/I_{2D}) deconvolve the intrinsic graphite quality and intrinsic disorder, respectively. All sample types stacking treated sample values over control sample types in clusters that begin on their respective days of evaluation aligned left to right as HOPG, artificial, natural, and PG(K&J) graphites (left-hand graph sets) and PG(UN), graphite rod, and felts GFA3 and GFA5 (right-hand graph sets).

graphene and graphites during air aging.[34−36,62,70−73] Since both peaks appeared in spectra of control and heat-treated samples, the observed increase in wetting of the treated samples, over their controls, would not seem to be moderated merely through surface-bound adventitious hydrocarbon (HC) and oxygen functional groups as previously reported.[34,36,70−72,74] Thus, the change in wetting properties of the treated samples may be explained through their electronic structure, including more than surface-bound functional group arrangements alone.[63,75,76] The hypothesis is that WCA most strongly reflects consistency with surface functional constituencies when they also correlate with electronic structural effects.

Micrographs reveal that some fibers in aged felts, which are fiber bundles, begin to separate into individual fibrils (Figure S4), increasing surface area and effective porosity of the felt. This degradation allows water to be forced through some areas of the felt (Video iv) but not others (Video v). Therefore, the wetting behavior of the aged graphite felts is not solely because of surface oxide accumulation during aging.[77] Thus, some combination of hydrophobic and hydrophilic fibers facilitated water penetration through the felt channels to increase the

DOI: 10.1021/acsanm.8b01887
ACS Appl. Nano Mater. 2019, 2, 228−240

overall porosity of the fibers, as seen from the CVs of the aged control fibers,[78] even though the hydrophilicity of these aged graphite felts was not sufficient enough to cause a buildup of non-Faradaic charges (capacitance increase).

Raman spectroscopy reveals both chemistry and morphology that may impact the electronic properties of graphites,[19] complementing both SEM imaging and ATR-FTIR spectroscopy.[64,79] When applied to investigate carbon materials, microRaman explores local properties including crystallinity[80] and defect density or disorder impacting the DOS,[64,79,80] which is important for HET.[19] The Raman spectra for HOPG show the so-called D band ca. 1350 cm^{-1}, characteristic of disorder and/or defects, in heat-treated samples but not the control (Figure 5) Additionally, peaks at ~1625 cm^{-1} appeared only for the spectra of the treated samples, which are identified with the D′ band. For other graphites employed in this research, both control and treated samples exhibit a D band, and all treated samples show the 1625 cm^{-1} D′ band as well as the graphite rod control (Figure S5). The D and D′ bands reflect the high DOS for zone-edge and midzone phonons, respectively.[80,81] All sample spectra have the 2D band at ~2720 cm^{-1}. The 2D band in graphite is due to graphite phonon backscattering and is dependent on the probing laser intensity and wavelength.[79]

Peak intensity (I) ratios of Raman bands provide an internally consistent and semiquantitative measure of disorder and other feature differences among similar materials and specifically herein track changes and stability over time. I_D/I_G is a measure of the disorder in the system. The common factor of I_D/I_G for the treated materials was consistently higher relative to their control samples. In natural graphite, graphite rod, and GFA5 (at day 63, end of experiment), control I_D/I_G values were higher than treated samples. To understand better what is happening, I_D/I_G was resolved into two different components

$$I_D/I_G = I_D/I_{2D} \times I_{2D}/I_G \quad (2)$$

Whereby, the I_D/I_{2D} is defined as the intrinsic defect density ratio, independent of the graphite (G) band. The I_{2D}/I_G value is suggestively dependent on changes in the graphite (G) component—without the I_D contribution—under constant incident laser power, which was approached through optical sample focus. Any inconsistencies in laser power impact only the 2D peak, leaving the D-to-G constant (I_{2D} is a strong indicator of the crystallinity in carbon materials and has been suggested as appropriate for relatively high-quality carbon determination).[82] All treated graphites show greater I_D/I_G, lower I_{2D}/I_G, and greater I_D/I_{2D} vs their control, indicating that increasing disorder is primarily responsible for material property enhancements, where G-band quality is preserved or even improved (Figure 6).

Conversely, the graphite mode is weaker in the control samples relative to their disorder species/structure content as probed by vibrational spectroscopy. This Raman analysis indicates thermally modulated restructuring in the treated samples. Natural graphite shows lower overall quality due to diminished G-band effects. The high I_{2D}/I_G of the graphite felts and the low I_D/I_{2D} imply that the higher I_D/I_G in the GFA5 control is not a function of more defects per se but of the graphite quality degradation over time (Figure S4). When all three trends are considered for the graphite rod, it is deduced that the now very porous nature and enhanced electrochemical properties, such as fast HET kinetics and symmetric capacitive behavior at fast scan rates, of the treated over the control graphite rods is because of the pronounced D′ band in the treated to the control ratio and less on the I_D/I_G as was previously thought. Thus, the treatment protocol fine-tuned the electronics of the graphite rod without drastic alteration of the defect density.

The in-plane crystallite spacing along the a-axis, L_a (in nm), values of the control and treated graphites were calculated from the Raman intensity ratio, I_D/I_G as previously proposed.[83]

$$L_a(\text{nm}) = (2.4 \times 10^{10})\lambda^4(I_D/I_G)^{-1} \quad (3)$$

Whereby λ is the wavelength (in nm) of the probing laser intensity employed in the Raman analysis (in this case, 532.5 nm). The results of the calculations for the control and treated samples at various days of the aging cycles are as shown in Table S1. The results show that besides the graphite rod and natural graphite, the L_a decreased for the treated groups in comparison with the control groups. The decrease in L_a between planes corresponds to an increase in crystallite sizes and transition to a lamellar structure from a diffusive one.[84,85] This corresponds to a well-ordered honeycomb-like structure with good electrical conductivity.[86] The deviation of the graphite rod from the trend is in tandem to the explanations given above for the I_D/I_G.

The D′ band and the higher D/G ratios in treated samples vs controls suggest an annealing that depends on the initial graphitic disorders to form, on average, with enhanced HET kinetics. Disorder in the controls is the foundation for structural and electronic reconfigurations on heat treatment. In addition, it has been reported that a certain degree of defect density is necessary for enhancing and even optimizing electrochemical and other electronics-based performance.[19] Intrinsic structural change altering the DOS, rather than surface chemistry and roughness, is the more important factor for improved HET rates.[87]

Four selected sample types—HOPG-ZYH, PG(K&J), GFA3, and artificial graphite—of the more dissimilar graphites analyzed with XPS reveal surface and near-sub-surface impacts of aging between control and treated samples freshly prepared (CF and TF) and fully aged (CA and TA). From XPS data for HOPG-ZYH, control and treated fresh samples (CF and TF) have significant amounts of sp^2-bonded carbons at 284.4 eV (Figure 7) while other graphites show that thermal treatment increased the sp^2 carbons over the sp^3 at ~285.6 eV (not shown). The results suggest that the oxides and Si (for the aged samples) groups did not modulate the fast HET kinetics in the treated samples (Figure S6). Summarily, thermal treatment increased the sp^2 content of the treated samples over their controls in some cases to ≥90% at start of the experiment. By the time of XPS analysis (~100 days from start of experiment), these sp^2 ratios were about 85%. From high-resolution XPS, the oxygen-containing species content of the TF GFA3 is 3.8 times greater than that of the CF sample. The treated and aged (TA) GFA3 had about 1.6 times the oxygen content of the treated and fresh (TF) sample just as the capacitance of the TA sample decreased to about half of those of the TF samples. This is also corroborated by the control and aged (CA) sample with roughly 90% of the oxygen content of the TF, and yet, it had no measurable capacitance (Figure S1). These results suggest that the surface-bound oxides, during aging, did not contribute to the capacitance of both the control and treated felts. These results suggest that the capacitance loss in the TA graphite felts, which could not have been

DOI: 10.1021/acsanm.8b01887
ACS Appl. Nano Mater. 2019, 2, 228−240

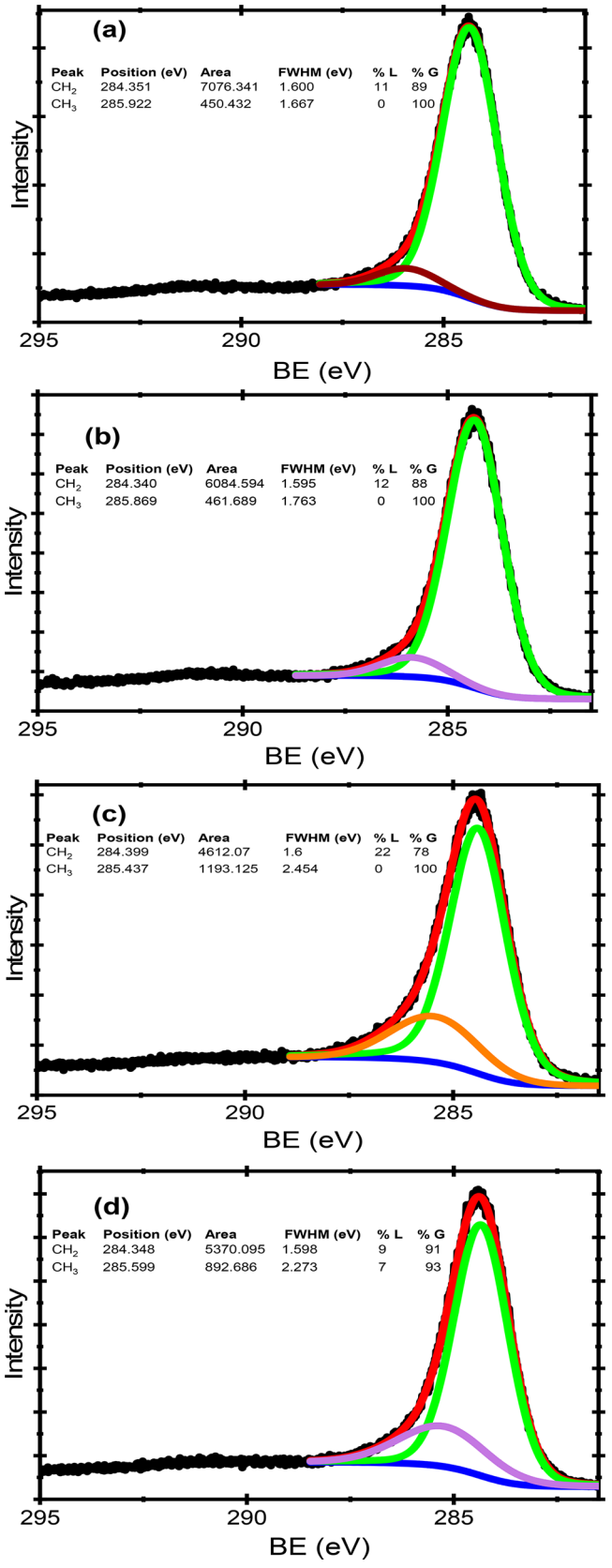

Figure 7. XPS plots of HOPG-ZYH samples for (a) treated and fresh HOPG-ZYH (C 1s), (b) control and fresh HOPG-ZYH (C 1s), (c) control and aged HOPG-ZYH (C 1s), and (d) treated and aged HOPG-ZYH (C 1s).

compensated by the surface-bound oxides during aging, is an indication that probably, sub-surface-bound oxygen is responsible for capacitance building. This would be true since the CA had appreciable oxygen content and capacitance of CF. These findings imply that harsh treatment protocols, such as excess heating or acid treatments,[77,88,89] used by most investigators may have masked the subtle but important impact of subsurface oxygen on both wetting and capacitance.

The XPS data from artificial graphite samples (TF and CF types) have similar sp^2 carbon compositions as their aged counterparts though their electrochemistry varied drastically (Table 1). Thus, the nature of the sp^2 carbon fractions for treated and control samples cannot be the same at the electroactive surface. For example, graphite felts at 90% sp^2 content had no appreciable wetting and facile HET kinetics.[90] This correlates with the fact that the high CH_2 content of these graphite felts did not influence their electronic nature to enhance their wettability and facile HET kinetics. A further example showed no correlation of electronic properties with sp^2 content in certain graphene oxides.[91] High sp^2 content alone does not guarantee facile HET kinetics or optimal electronic properties.

UPS provides valence-band spectra for HOMO-level chemical materials analysis toward understanding the relationship of the sp^2 content with optimal electronic properties such as facile HET and increased capacitance. From previous UPS works, the He_1 (21.2 eV) and He_2 (40.2 eV) lines for graphites[92,93] help to interpret HOPG valence-band spectra (Figure 8) and the valence bands of artificial graphites, GFA3 and PG(K&J) (the spectral lines of the He_1 and He_2 of the graphites studied in this research yielded similar interpretations).

The UPS plots of HOPG-ZYH control (C) and treated (T) samples comparing fresh (F) and aged (A) states (Figure 8) indicating the propensity of their π over σ interactions (or vice versa) is interrogated using the intensity ratios, $(I_{\pi i}/I_{\sigma i})$ at certain π and σ regions.[94]

Peak P_1* is due to the high DOS in the Brillouin zone,[92] which may be explained in the context of the band-structure calculation with the width of the valley reflecting the separation of $\sigma 2$ and $\sigma 3$ bands at the symmetry point P. The parameter $\Delta(\sigma 2-\sigma 3)$, measured at half of the well depth, reflects the nearness of $\sigma 2$ and $\sigma 3$ bonds such that a smaller value is a closer attraction and greater repulsion, where σ bonds are treated as point charges (Figure 8a).

Larger $\Delta(\sigma 2-\sigma 3)$ values indicate decreased magnitude of Coulombic interaction. The Δh reflects energy well depths positively correlated with greater σ bond interaction strength,[95] stability,[96] and even molecular size.[97] The present work reveals (a) higher DOS near P_1* (as the intensity at P_1*) in treated vs control analogues (Table 2) and demonstrates a higher density of phonon states of the treated to the control and (b) an increase of the $\Delta(\sigma 2-\sigma 3)$ for treated over control. This means a decreased magnitude of Coulombic interaction for the treated analogues over the controls. (c) An increase in Δh for control over treated analogues implies the greater σ bond interaction strength and stability and (d) an overall increase in $I_{\pi i}/I_{\sigma i}$ of treated vs control analogues, which means the overall increase in the propensity for π bond formation over those of the σ bonds.

Additionally, the treated samples have either a higher HOMO or DOS at the valence-band maximum relative to the controls [a prominent exception is the higher DOS of CF

DOI: 10.1021/acsanm.8b01887
ACS Appl. Nano Mater. 2019, 2, 228−240

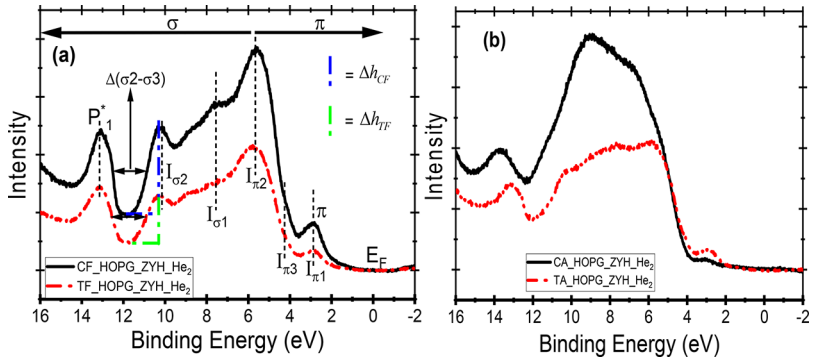

Figure 8. (a) Valence-band spectra of fresh control (CF) and heat-treated (TF) HOPG. The blue and green vertical lines on the right are used to depict the heights, Δh_{CF} and Δh_{TF}, respectively, of the energy wells in the diagram; (b) valence-band spectra of aged samples. Spectral lines emanate from the He_2 excitation lines.

Table 2. Ratios of the Intensities of the π to σ Transitions in the He_1 and He_2 Excitation Lines of the Control and Treated HOPG-ZYH

	He_1 (21.2 eV)			
	$I_{\pi 2}/I_{\sigma 1}$	$I_{\pi 2}/I_{\sigma 2}$	$I_{P_1*}/I_{\sigma 2}$	$I_{\pi 1}/I_{\sigma 1}$
CF_HOPG-ZYH	1.3535	1.5638	0.9788	0.2845
TF_HOPG-ZYH	1.4087	1.6629	1.1094	0.2166
CA_HOPG-ZYH	0.8667	1.0981	0.6526	0.0463
TA_HOPG-ZYH	1.0197	1.2705	0.8582	0.1657
	He_2 (40.8 eV)			
	$I_{\pi 2}/I_{\sigma 1}$	$I_{\pi 2}/I_{\sigma 2}$	$I_{P_1*}/I_{\sigma 2}$	$I_{\pi 1}/I_{\sigma 1}$
CF_HOPG-ZYH	1.5823	1.6010	1.6845	0.2467
TF_HOPG-ZYH	1.4190	1.6758	1.5323	0.1419
CA_HOPG-ZYH	0.8051	1.3042	0.9141	0.0323
TA_HOPG-ZYH	0.9170	1.1353	1.0711	0.0921

HOPG at E_F than in the treated samples, which is diminished for the CA sample (Figure 8)] or were roughly the same. However, irrespective of the nature of their HOMOs, the control samples had deeper and more greatly interacting σ bond energy wells compared to the treated samples. On the other hand, the treated sample spectra had pronounced π bonds relative to the controls. This suggests that the prominence of the DOS at the HOMO may not be the primary factor for the enhanced electronic response of heat-treated materials but an overall higher DOS, compared to their controls, and localized on the π bonds. These π bonds, being delocalized, have greater probabilities for conduction.[98] A drastic increase in DOS, as viewed by UPS, of the π bonds and E_F at 600−650 °C of the graphene oxide species was also reported,[91] even though the XPS results did not differentiate between low and high DOS sp^2.

When coherently analyzed, the sp^2 nature in the treated materials are conjugating with high DOS localized on the π bonds. Hence, heat treatment resulted in a structural reorganization at the molecular level of the graphite resulting also in tuning the electronic nature to enhance electrochemical behavior as depicted in Scheme 1. The degree of change possible is dependent on the initial disordered state as well as on the final structural and electronic condition. Less disorder in HOPG-ZYH relative to other studied graphites would account for its accelerated aging in comparison. There exists a balance between the formation of disordered regions, clearly seen in the D′ band, that contribute to the high density of energy states and the degree of crystallinity along the lattice sites that enable carrier hopping.

These findings suggest the same and or very similar underlying mechanism(s) to the formation of the end structure after thermal treatment. Heat treatment results in a well-ordered state, which when described via the folding funnel model,[39−41] implies that there exists a path to a minimum ΔG of crystallinity irrespective of the starting graphite material (with respect to the graphite employed in our work) such that the new microscopic graphite state is mainly aromatic with a degree of crystallinity along the lattice sites that enable carrier hopping irrespective of adventitious oxygen-containing and hydrocarbon moieties, synonymous with aging-induced sluggish electron transfer kinetics. This then suggests that the electronic structure is unperturbed signifying a diminution of Coulombic (repulsive) contributive forces. This carrier hopping, from site-to-site, would be aromatic (sp^2 hybridized)

Scheme 1. Thermal Treatment Protocol of the Pristine Graphite (Before) for Enhanced and Sustained HET (After)[a]

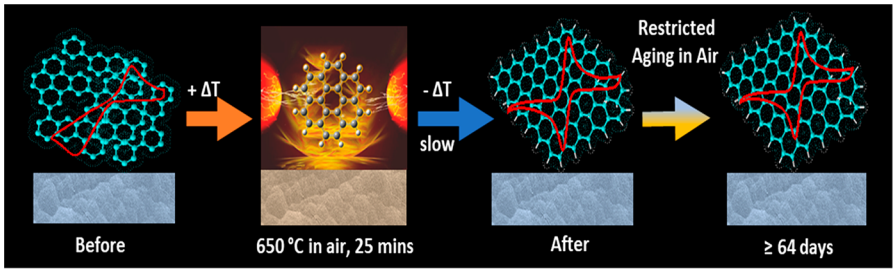

[a]Thermal treatment results in structural and electronic reconfigurations without surface morphological changes (before vs after). The consequence of this restructuring is that sluggish HET kinetics (before) becomes fast (after) and is sustained afterwards (≥ 64 days).

DOI: 10.1021/acsanm.8b01887
ACS Appl. Nano Mater. 2019, 2, 228−240

with delocalizing π electrons. This suggests that the new microscopic graphitic states are mainly aromatic with a degree of crystallinity favoring enhanced and sustained electron transport. The implication is an electronic structure unperturbed by oxygen or HC surface functional group contaminants for a diminished Coulombic contribution. The attributes of this electronic structure demonstrate a strongly correlated system, exhibiting nonperturbative behavior.[99] The one-dimensional Hubbard model[42] describes this nonperturbative behavior, explaining the surface-to-electronic chemistry of treated graphite materials in addressing both their enhanced electrochemical performance and depressed aging effects. The consequences of the thermally induced microstructures and strongly correlated electronic structures could be used to explain the wetting characteristics of the thermally treated graphites over those of the controls.

Thus, to describe the wetting behavior of the treated materials (now assumed to be nonperturbative) and their resistance to aging, it is postulated that the electric fields of polar molecules such as water[37] are sensitive to the electron cloud of the correlated π system. Tribological charging is well-known to produce large electrostatic effects[100−102] when a graphite block is peeled to reveal a fresh surface[102] that can be wet out to zero WCA even where the fully discharged material is known to be hydrophobic. Adventitious HC can dissipate excess π electrons to form sp^3-bonded carbon[103,104] or utilize tribo-charges to form sp^2-bonded methylene groups to the graphite surface, also damping the electronics and increasing the WCA. Thermally treated graphite, possessing a well-correlated, nonperturbed electronic nature, is shielded from the influence of the HC or oxygen groups via a mechanism well-illustrated by the Hubbard model, so that the π electron clouds are unperturbed (see Supporting Information).

CONCLUSIONS

A new thermal treatment protocol for graphites resulted in steady and consistent ΔE_p values from aqueous cyclic voltammetry over 64 days with no appreciable aging from air oxidation on storage. The initially enhanced and sustained heterogeneous rate constants of graphite samples when probed with the $Fe(CN)_6^{3-/4-}$ redox couple remains essentially unchanged over the test periods. All graphite types exhibit the same resistance to aging and very similar behaviors relative to their controls through results from FTIR, Raman, XPS, UPS, and water contact angle measurements. The facile and sustained HET kinetics in 1 mM ferri-ferrocyanide solution is attributable to structural and electronic changes and not from surface functional group changes or edge-density contributions.

These findings suggest that the same or very similar underlying mechanism(s) via thermal treatment promote a more stable structure as a well-ordered or higher-order state (e.g., mainly aromatic, crystalline microstates) than the original graphites, being described by the folding funnel model.[39−41] This new graphite state, or ensemble, possesses a degree of crystallinity along the lattice sites that enables carrier hopping irrespective of adventitious oxygen-containing and hydrocarbon moieties synonymous with aging-induced sluggish electron transfer kinetics. This then suggests that the electronic structure is less perturbed and signifies a reduction of Coulombic (repulsive) contributions. The one-dimensional Hubbard model[42] explains the surface-to-electronic chemistry of heat-treated graphite materials having enhanced and sustained electronic/electrochemical properties compared to their controls regardless of any adventitious functional surface groups indicated or even those changes that would remain potentially undetected as below the limits of investigation.

Water contact angles reveal sensitivity to the electronic nature of the treated graphites as distinct from the expected surface chemistry effects. Additionally, capacitance of graphite felts arise from subsurface and not surface-bound oxygen-containing species as previously suggested. The overall increase in DOS with enhanced and delocalized π over σ traits cause electronic property enhancements in the treated graphites. Chemical structural disorder in graphite provides preferential initiation sites for the thermally induced structural and electronic reorganization in the treated samples. On the basis of the fast and sustained HET kinetics of the thermally treated graphite electrode materials, this new treatment protocol can be used in applications hinging on fast electron transfer and/or increased capacitance, such as sensing, electro-oxidative reactions in water purification, batteries and supercapacitors, catalysis, oxygen reduction for fuel cells, HPLC detectors, and semiconductors.

METHODS

Chemicals and Materials. All chemicals were used as received from the suppliers. HOPG ZYH block (NT-MDT Spectrum Instruments, Inc.). Natural graphite (T62) (50 × 20 × 0.13 mm^3) and artificial graphite sheets (T68) (50 × 20 × 25 μm) were gifts (t-Global Technology Co. Ltd., Taiwan). Pyrolytic graphite blocks, PG1 (32 ± 2 × 16 ± 2 × 0.75 ± 0.5 mm) (K & J Magnetics [Plumsteadville, PA, USA]) and pyrolytic graphite blocks (United Nuclear [Laingsburg, MI, USA]). Graphite rods (40767-KD: graphite rod, 6.15 mm (0.242 in) diameter ×152 mm (6 in) long, 99.9995% (metals basis) (Alfa Aesar [Haverhill, MA, USA]). Graphite blocks (99.99%, 40 × 40 × 3 mm^3 thick) (Fujiansheng, China). Ag/AgCl/3 M NaCl (aq) reference electrodes (0.209 V vs SHE) and reference electrode cells [Bioanalytical Systems Inc. (BASi), (West Lafayette, IN, USA)]. Battery Felt SIGRACELL GFA3 (297 × 210 × 3 mm^3 thick) and Soft Felt SIGRATHERM GFA5 (297 × 210 × 5 mm^3 thick) were gifts (SGL Carbon Company GmbH, Postfach, Meitingen, Germany).

Potassium hexacyanoferrate (III) ($Fe(CN)_6^{3/4-}$; ACS reagent, ≥99.0%) and potassium chloride crystal (SigmaUltra; > 99.0%, Sigma Chemical Co., [St. Louis, MO, USA]). Advanced abrasives (Sand-Blaster, 3 M [St. Paul, MN, USA]); Teflon tape (Dupont, Elk Grove Village, IL, USA).

The high-temperature furnace was a Lindberg/Blue M type model [Thermo Scientific (Asheville NC, USA)]. All chemicals were used as received, and all aqueous stock solutions were prepared with Milli-Q (18 MΩ) water.

Sample Preparation. Graphite rods were cut into small pieces, and their ends were polished with a 100 grit sandblaster followed by a finishing polishing with a 320 grit sandblaster. The final lengths of the finished products were 1 to 2 cm. The artificial graphite was peeled off from its nylon protective wrap and used as is. The natural graphite and graphite felts (GFA3 and GFA5) were used as received. The PG blocks were exfoliated using Scotch tape to expose fresh and pristine surfaces prior to thermal treatment and or the start of control experiments using these pristine surfaces. The HOPG-ZYH was peeled off its block using Scotch tape.

Thermal Treatment. Samples loaded onto a ceramic block were inserted into a quartz tube furnace preheated to 650 °C, exposed to air at both ends, and heated for 25 min. Then the furnace was turned off, cooled to ∼500 °C in ∼15 min, and further cooled to ∼200 °C with its hatches left open until the samples were removed. Scheme 1 also depicts the thermal synthesis protocol.

SEM Imaging. Scanning electron microscope (SEM) images for the pristine (control) and freshly treated samples were obtained with

DOI: 10.1021/acsanm.8b01887
ACS Appl. Nano Mater. 2019, 2, 228−240

a JEOL 2010J 200 kV Analytical TEM/STEM, with a vacuum pressure of less than 10^{-6} Torr. Images were obtained at various magnifications.

Aging in Air. The control graphite samples for air aging (artificial and natural graphites, GFA3 and GFA5) were used as is from the suppliers. However, they were only unwrapped and exposed to air immediately at the point of starting the aging experiments. The surfaces of the pyrolytic graphite were renewed by peeling off several graphene layers via the Scotch tape method.[105] HOPG-ZYH was peeled off fresh via the Scotch tape method and thus used fresh for the aging experiments. At the beginning of the aging experiment, the surface of the graphite rod was cleaned by polishing slightly using a 320 grit (very fine) sandblaster.

No additional processing for surface regeneration of the heated graphite samples prior to the start of experiment was required. The surfaces used for thermal treatment were then left exposed to air for the period of the aging experiment.

Aging in 1 mM $[Fe(CN)_6]^{3-/4-}$ (1 M KCl). Freshly exfoliated PG blocks (controls) as well as thermally treated samples were formed into electrodes and left in solutions of 1 mM $[Fe(CN)_6]^{3-/4-}$ (1 M KCl) for the duration of the experiments. Cyclic voltammograms of the electrodes were recorded at start and end of the experiment.

Contact Angle Measurements. Contact angle measurements were carried out using a Model 250-U1 Ramé-Hart goniometer (Succasunna, NJ, USA) with illumination provided by a Ramé-Hart 150w Fiber Optic illuminator (Model FOI-150-UL). Images were captured using a Ramé-Hart live stream camera with a CCD. Single volumes of 2 μL were automatically dispensed via a model p/n 100–22 Ramé-Hart auto dispensing system. Both the goniometer and auto dispenser were automatically controlled via DROPimage Advanced software (version 2.10.01) with the capability of taking pictures and processing images for contact angle measurements. For expediency, static contact angles were measured, as the generally accepted approximate for the more proper advancing contact angle, by spotting 2 μL volumes on at least five different spots on both sides of each graphite material studied. The DROPimage software provided digital processing for precise contact angle determination. The average of the angles for all spots photographed served as the contact angle for any given sample measurement. The humidity of the environment during these measurements ranged from 20 to 55% and temperatures from 20 to 23 °C.

For treated graphite rods, graphite felts and natural graphite with strong wetting, dynamic contact angles were recorded via the DROPimage Advanced software trigger command.

Attenuated Total Reflection (ATR)-FTIR. Attenuated total reflection (ATR)-Fourier transform infrared (FTIR) spectroscopy was performed using a Thermo Scientific Nicolet iS 10 FT-IR spectrometer with the Smart iTR accessory. The crystal plate was diamond with a ZnSe lens. The samples were clamped onto the crystal plate and lens using the pressure tower. A total of 64 spectral scans were averaged to generate a spectrum for any point on the desired graphite material. Spectral scans were recorded on a minimum of three different spots on both sides of the graphite surfaces.

Raman Spectroscopy. Raman scattering spectra were collected with a WITec alpha300 R Raman instrument (GmbH, Germany): A 100 mW, frequency doubled, Nd:YAG (λ = 532.5 nm) laser focused through a 20× Nikon objective (NA = 0.4, WD = 3.9 mm) creates a spot size of ~10 μm. The laser power was attenuated manually to reduce fluorescence background and thermal effects during the first 2 weeks of measurements to achieve a sufficient signal-to-noise ratio to distinguish graphite bands of all sample types with qualitative similarity, giving a final incident sample irradiation power on the order of 10 mW across all samples in all weeks, considering sample-day variations that are not precisely controllable. After week 2, the laser power was never adjusted. Single spectrum "spot" scans were acquired using the alpha300 R via a UHT-300 spectrometer (grating = 600 grooves/mm, entrance aperture = 50 μm), with the Andor DU970N–BV, 1600 × 200 pixel, CCD array detector. Each Raman spectrum was an average of 10 spectral accumulations at 0.50 s integration time. Optical images were saved from each sample area interrogated. Raman measurements, for samples that had some degree of visible defects, were done on the defect-free surfaces as judged from the optical images now acquired.

X-ray Photoelectron Spectroscopy (XPS) and Ultraviolet Photoelectron Spectroscopy (UPS). XPS, or electron spectroscopy for chemical analysis (ESCA), measurements occurred in an ultrahigh vacuum (UHV) with a base pressure $<10^{-10}$ Torr using a dual anode X-ray source, XR 04–548 (Physical Electronics), and an Omicron EA 125 hemispherical energy analyzer with a resolution of 0.02 eV. The X-ray source was the Al Kα source operated at 400 W and an X-ray incident angle of 54.7° and normal emission. A freshly exfoliated HOPG-ZYH sample served as the reference spectrum for the C 1s binding energy.

XPS Peak 4.1 software provided the peak fitting, while peak quantifications came from both XPS Peak 4.1 and Origin version 2018b. The background type, using XPSPEAK41, was Shirley.

UPS spectra were acquired with the same analyzer as the XPS, using both He I (21.2 eV) and He II (40.8 eV) excitation lines.

Cyclic Voltammetry. Cyclic voltammetry of the various carbon materials as working electrodes was performed with a VersaStat 3 potentiostat/galvanostat (Princeton Applied Research). The working electrodes were the graphite materials investigated, while a graphite block (99.99%, 40 × 40 × 3 mm^3 thick) served as the counter electrode, and Ag/AgCl (3 M NaCl) was the reference electrode. The electrolyte was a 1 mM $[Fe(CN)_6]^{3-/4-}$ (1 M KCl) solution.

Data Processing. All data were processed using both Microsoft Excel 2016 and Origin version 2018b software. All graphs were plotted using the Origin version 2018b graph plotting component.

■ ASSOCIATED CONTENT

Supporting Information

The Supporting Information is available free of charge on the ACS Publications website at DOI: 10.1021/acsanm.8b01887.

More information on the CVs and SEM micrographs of other graphites employed in this work. Additionally, the micrographs of aged and control graphite felts showing areas of differential wetting and their SEM micrographs highlighting areas of bundle splitting, thus, permitting porosity. The Raman spectra of the other graphite materials. Insets in these Raman spectra are the magnifications of their G bands to reveal the D′ bands' occurrence in the treated. The Hubbard model employed to explain the surface-to-electronic structure of the thermally treated graphite.(PDF)

Video i: Video showing the total wetting (0°) of the treated graphite felt (AVI)

Video ii: Video showing the porosity of treated natural graphite (AVI)

Video iii: Video showing the porosity of treated graphite rod (AVI)

Video iv: Video shows that degradation allows water to be forced through some areas of the felt but not others (AVI)

Video v: Same graphite felt type as Video iv resisting water impregnation (AVI)

■ AUTHOR INFORMATION

Corresponding Author

*E-mail: aston@uidaho.edu.

ORCID

Jean'ne M. Shreeve: 0000-0001-8622-4897

D. Eric Aston: 0000-0002-5189-4302

Notes

The authors declare no competing financial interest.

DOI: 10.1021/acsanm.8b01887
ACS Appl. Nano Mater. 2019, 2, 228–240

■ ACKNOWLEDGMENTS

OCN appreciates research funding from the College of Science Dean's Office and recognizes the Integrated Research and Innovation Center (IRIC) at the University of Idaho. L. Scudiero of the Dept. of Chemistry and Material Science and Engineering Program at Washington State University is warmly thanked for helpful discussions on photoelectron spectroscopy.

■ REFERENCES

(1) Chandra, S.; Miller, A. D.; Bendavid, A.; Martin, P. J.; Wong, D. K. Y. Minimizing Fouling at Hydrogenated Conical-Tip Carbon Electrodes during Dopamine Detection in Vivo. *Anal. Chem.* **2014**, *86*, 2443−2450.

(2) Velický, M.; Bradley, D. F.; Cooper, A. J.; Hill, E. W.; Kinloch, I. A.; Mishchenko, A.; Novoselov, K. S.; Patten, H. V.; Toth, P. S.; Valota, A. T.; Worrall, S. D.; Dryfe, R. A. W. Electron Transfer Kinetics on Mono- and Multilayer Graphene. *ACS Nano* **2014**, *8*, 10089−10100.

(3) Hu, L.; Peng, X.; Huo, K.; Chen, R.; Fu, J.; Li, Y.; Lee, L. Y. S.; Wong, K.-Y.; Chu, P. K. Dominant Factors Governing the Electron Transfer Kinetics and Electrochemical Biosensing Properties of Carbon Nanofiber Arrays. *ACS Appl. Mater. Interfaces* **2016**, *8*, 28872−28879.

(4) Sofer, Z.; Jankovský, O.; Šimek, P.; Sedmidubský, D.; Šturala, J.; Kosina, J.; Mikšová, R.; Macková, A.; Mikulics, M.; Pumera, M. Insight into the Mechanism of the Thermal Reduction of Graphite Oxide: Deuterium-Labeled Graphite Oxide Is the Key. *ACS Nano* **2015**, *9*, 5478−5485.

(5) Mao, X.; Guo, F.; Yan, E. H.; Rutledge, G. C.; Hatton, T. A. Remarkably High Heterogeneous Electron Transfer Activity of Carbon-Nanotube-Supported Reduced Graphene Oxide. *Chem. Mater.* **2016**, *28*, 7422−7432.

(6) Parker, J. F.; Kamm, G. E.; McGovern, A. D.; Desario, P. A.; Rolison, D. R.; Lytle, J. C.; Long, J. W. Rewriting Electron-Transfer Kinetics at Pyrolytic Carbon Electrodes Decorated with Nanometric Ruthenium Oxide. *Langmuir* **2017**, *33*, 9416−9425.

(7) Taylor, S. M.; Pătru, A.; Perego, D.; Fabbri, E.; Schmidt, T. J. Influence of Carbon Material Properties on Activity and Stability of the Negative Electrode in Vanadium Redox Flow Batteries: A Model Electrode Study. *ACS Appl. Energy Mater.* **2018**, *1*, 1166−1174.

(8) Ferrari, A. C.; Bonaccorso, F.; Fal'ko, V.; Novoselov, K. S.; Roche, S.; Bøggild, P.; Borini, S.; Koppens, F. H. L.; Palermo, V.; Pugno, N.; et al. Science and Technology Roadmap for Graphene, Related Two-Dimensional Crystals, and Hybrid Systems. *Nanoscale* **2015**, *7*, 4598−4810.

(9) Kong, Y.; Wang, Z.-L.; Wang, Y.; Yuan, J.; Chen, Z.-D. Degradation of Methyl Orange in Artificial Wastewater through Electrochemical Oxidation Using Exfoliated Graphite Electrode. *Xinxing Tan Cailiao/New Carbon Mater.* **2011**, *26*, 459−464.

(10) Maljaei, A.; Arami, M.; Mahmoodi, N. M. Decolorization and Aromatic Ring Degradation of Colored Textile Wastewater Using Indirect Electrochemical Oxidation Method. *Desalination* **2009**, *249*, 1074−1078.

(11) McCreery, R. L.; McDermott, M. T. Comment on Electrochemical Kinetics at Ordered Graphite Electrodes. *Anal. Chem.* **2012**, *84*, 2602−2605.

(12) McCreery, R. L. Advanced Carbon Electrode Materials for Molecular Electrochemistry. *Chem. Rev.* **2008**, *108*, 2646−2687.

(13) Brownson, D. A. C.; Kampouris, D. K.; Banks, C. E. Graphene Electrochemistry: Fundamental Concepts through to Prominent Applications. *Chem. Soc. Rev.* **2012**, *41*, 6944.

(14) Song, Y.; Hu, H.; Feng, M.; Zhan, H. Carbon Nanotubes with Tailored Density of Electronic States for Electrochemical Applications. *ACS Appl. Mater. Interfaces* **2015**, *7*, 25793−25803.

(15) Chen, S.; Liu, Y.; Chen, J. Heterogeneous Electron Transfer at Nanoscopic Electrodes: Importance of Electronic Structures and Electric Double Layers. *Chem. Soc. Rev.* **2014**, *43*, 5372−5386.

(16) Barbieri, P. F.; Marques, F. C. The Effect of Stress in the Density of States of Amorphous Carbon Films Determined by X-Ray Excited Auger Electron Spectroscopy. *Adv. Mater. Sci. Eng.* **2017**, *2017*, 1.

(17) Unwin, P. R.; Güell, A. G.; Zhang, G. Nanoscale Electrochemistry of Sp2 Carbon Materials: From Graphite and Graphene to Carbon Nanotubes. *Acc. Chem. Res.* **2016**, *49*, 2041−2048.

(18) McDermott, M. T.; Kneten, K.; McCreery, R. L. Anthraquinonedisulfonate Adsorption, Electron-Transfer Kinetics, and Capacitance on Ordered Graphite Electrodes: The Important Role of Surface Defects. *J. Phys. Chem.* **1992**, *96*, 3124−3130.

(19) Zhong, J. H.; Zhang, J.; Jin, X.; Liu, J. Y.; Li, Q.; Li, M. H.; Cai, W.; Wu, D. Y.; Zhan, D.; Ren, B. Quantitative Correlation between Defect Density and Heterogeneous Electron Transfer Rate of Single Layer Graphene. *J. Am. Chem. Soc.* **2014**, *136*, 16609−16617.

(20) Sun, T.; Levin, B. D. A.; Guzman, J. J. L.; Enders, A.; Muller, D. A.; Angenent, L. T.; Lehmann, J. Rapid Electron Transfer by the Carbon Matrix in Natural Pyrogenic Carbon. *Nat. Commun.* **2017**, *8*, 14873.

(21) Štulík, K. Activation of Solid Electrodes. *Electroanalysis* **1992**, *4*, 829−834.

(22) Swain, G. M. Solid Electrode Materials: Pretreatment and Activation. In *Handbook of Electrochemictry*, 1st ed.; Zoski, C. G., Ed.; Elsevier B.V.: Amsterdam, 2007; pp 111−153.

(23) Shrestha, S.; Morse, N.; Mustain, W. E. Effect of Surface Chemistry on the Double Layer Capacitance of Polypyrrole-Derived Ordered Mesoporous Carbon. *RSC Adv.* **2014**, *4*, 47039−47046.

(24) Ramani, M.; Haran, B. S.; White, R. E.; Popov, B. N.; Arsov, L. Studies on Activated Carbon Capacitor Materials Loaded with Different Amounts of Ruthenium Oxide. *J. Power Sources* **2001**, *93*, 209−214.

(25) Ruiz, V.; Blanco, C.; Raymundo-Piñero, E.; Khomenko, V.; Béguin, F.; Santamaría, R. Effects of Thermal Treatment of Activated Carbon on the Electrochemical Behaviour in Supercapacitors. *Electrochim. Acta* **2007**, *52*, 4969−4973.

(26) Sánchez-González, J.; Stoeckli, F.; Centeno, T. A. The Role of the Electric Conductivity of Carbons in the Electrochemical Capacitor Performance. *J. Electroanal. Chem.* **2011**, *657*, 176−180.

(27) Bowling, R. J.; Packard, R. T.; McCreery, R. L. Activation of Highly Ordered Pyrolytic Graphite for Heterogeneous Electron Transfer: Relationship between Electrochemical Performance and Carbon Microstructure. *J. Am. Chem. Soc.* **1989**, *111*, 1217−1223.

(28) Poon, M.; McCreery, R. L.; Engstrom, R. Laser Activation of Carbon Electrodes. Relationship between Laser-Induced Surface Effects and Electron Transfer Activation. *Anal. Chem.* **1988**, *60*, 1725−1730.

(29) Batrakov, A. V.; Markov, A. B.; Ozur, G. E.; Proskurovsky, D. I.; Rotshtein, V. P. The Effect of Pulsed Electron-Beam Treatment of Electrodes on Vacuum Breakdown. *IEEE Trans. Dielectr. Electr. Insul.* **1995**, *2*, 237−242.

(30) Malmgren, S.; Ciosek, K.; Lindblad, R.; Plogmaker, S.; Kühn, J.; Rensmo, H.; Edström, K.; Hahlin, M. Consequences of Air Exposure on the Lithiated Graphite SEI. *Electrochim. Acta* **2013**, *105*, 83−91.

(31) Ranganathan, S.; Kuo, T.; Mccreery, R. L. Facile Preparation of Active Glassy Carbon Electrodes with Activated Carbon and Organic Solvents. *Anal. Chem.* **1999**, *71*, 3574−3580.

(32) Chen, P.; Fryling, M. A.; McCreery, R. L. Electron Transfer Kinetics at Modified Carbon Electrode Surfaces: The Role of Specific Surface Sites. *Anal. Chem.* **1995**, *67*, 3115−3122.

(33) Ji, X.; Banks, C. E.; Crossley, A.; Compton, R. G. Oxygenated Edge Plane Sites Slow the Electron Transfer of the Ferro-/Ferricyanide Redox Couple at Graphite Electrodes. *ChemPhysChem* **2006**, *7*, 1337−1344.

(34) Martinez-Martin, D.; Longuinhos, R.; Izquierdo, J. G.; Marele, A.; Alexandre, S. S.; Jaafar, M.; Gómez-Rodríguez, J. M.; Bañares, L.; Soler, J. M.; Gomez-Herrero, J. Atmospheric Contaminants on Graphitic Surfaces. *Carbon* **2013**, *61*, 33−39.

(35) Kozbial, A.; Zhou, F.; Li, Z.; Liu, H.; Li, L. Are Graphitic Surfaces Hydrophobic? *Acc. Chem. Res.* **2016**, *49*, 2765−2773.

DOI: 10.1021/acsanm.8b01887
ACS Appl. Nano Mater. 2019, 2, 228−240

(36) Li, Z.; Kozbial, A.; Nioradze, N.; Parobek, D.; Shenoy, G. J.; Salim, M.; Amemiya, S.; Li, L.; Liu, H. Water Protects Graphitic Surface from Airborne Hydrocarbon Contamination. *ACS Nano* **2016**, *10*, 349−359.
(37) Misra, R. P.; Blankschtein, D. Insights on the Role of Many-Body Polarization Effects in the Wetting of Graphitic Surfaces by Water. *J. Phys. Chem. C* **2017**, *121*, 28166−28179.
(38) Morteza Najarian, A.; Chen, R.; Balla, R. J.; Amemiya, S.; McCreery, R. L. Ultraflat, Pristine, and Robust Carbon Electrode for Fast Electron-Transfer Kinetics. *Anal. Chem.* **2017**, *89*, 13532−13540.
(39) Leopold, P. E.; Montal, M.; Onuchic, J. N. Protein Folding Funnels: A Kinetic Approach to the Sequence-Structure Relationship. *Proc. Natl. Acad. Sci. U. S. A.* **1992**, *89*, 8721−8725.
(40) Bryngelson, J. D.; Onuchic, J. N.; Socci, N. D.; Wolynes, P. G. Funnels, Pathways, and the Energy Landscape of Protein Folding: A Synthesis. *Proteins: Struct., Funct., Genet.* **1995**, *21*, 167−195.
(41) Onuchic, J. N.; Socci, N. D.; Luthey-Schulten, Z.; Wolynes, P. G. Protein Folding Funnels: The Nature of the Transition State Ensemble. *Folding Des.* **1996**, *1*, 441−450.
(42) Hubbard, J. Electron Correlations in Narrow Energy Bands. *Proc. R. Soc. London, Ser. A* **1963**, *276*, 238−257.
(43) Hu, L.; Peng, X.; Huo, K.; Chen, R.; Fu, J.; Li, Y.; Lee, L. Y. S.; Wong, K.-Y.; Chu, P. K. Dominant Factors Governing the Electron Transfer Kinetics and Electrochemical Biosensing Properties of Carbon Nanofiber Arrays. *ACS Appl. Mater. Interfaces* **2016**, *8*, 28872−28879.
(44) Zhang, G.; Tan, S.; Patel, A. N.; Unwin, P. R. Electrochemistry of $Fe^{3+/2+}$ at Highly Oriented Pyrolytic Graphite (HOPG) Electrodes: Kinetics, Identification of Major Electroactive Sites and Time Effects on the Response. *Phys. Chem. Chem. Phys.* **2016**, *18*, 32387−32395.
(45) Güell, A. G.; Cuharuc, A. S.; Kim, Y. R.; Zhang, G.; Tan, S. Y.; Ebejer, N.; Unwin, P. R. Redox-Dependent Spatially Resolved Electrochemistry at Graphene and Graphite Step Edges. *ACS Nano* **2015**, *9*, 3558−3571.
(46) Nicholson, R. S. Theory and Application of Cyclic Voltammetry f m Measurement of Electrode Reaction Kinetics. *Anal. Chem.* **1965**, *37*, 1351−1355.
(47) Konopka, S. J.; McDuffie, B. Diffusion Coefficients of Ferri- and Ferrocyanide Ions in Aqueous Media, Using Twin-Electrode Thin-Layer Electrochemistry. *Anal. Chem.* **1970**, *42*, 1741−1746.
(48) Poler, J. C. Surface Oxidation Kinetics: A Scanning Tunneling Microscopy Experiment. *J. Chem. Educ.* **2000**, *77*, 1198−1200.
(49) Stevens, F.; Kolodny, L. a.; Beebe, T. P. Kinetics of Graphite Oxidation: Monolayer and Multilayer Etch Pits in HOPG Studied by STM. *J. Phys. Chem. B* **1998**, *102*, 10799−10804.
(50) Gonçalves, L. M.; Batchelor-Mcauley, C.; Barros, A. A.; Compton, R. G. Electrochemical Oxidation of Adenine: A Mixed Adsorption and Diffusion Response on an Edge-Plane Pyrolytic Graphite Electrode. *J. Phys. Chem. C* **2010**, *114*, 14213−14219.
(51) Zhang, G.; Kirkman, P. M.; Patel, A. N.; Cuharuc, A. S.; McKelvey, K.; Unwin, P. R. Molecular Functionalization of Graphite Surfaces: Basal Plane versus Step Edge Electrochemical Activity. *J. Am. Chem. Soc.* **2014**, *136*, 11444−11451.
(52) Davies, T. J.; Hyde, M. E.; Compton, R. G. Nanotrench Arrays Reveal Insight into Graphite Electrochemistry. *Angew. Chem., Int. Ed.* **2005**, *44*, 5121−5126.
(53) Tang, C.; Zhang, Q. Nanocarbon for Oxygen Reduction Electrocatalysis: Dopants, Edges, and Defects. *Adv. Mater.* **2017**, *29*, 1604103.
(54) Yuan, W.; Zhou, Y.; Li, Y.; Li, C.; Peng, H.; Zhang, J.; Liu, Z.; Dai, L.; Shi, G. The Edge- and Basal-Plane-Specific Electrochemistry of a Single-Layer Graphene Sheet. *Sci. Rep.* **2013**, *3*, 2248.
(55) Patel, A. N.; Tan, S. Y.; Miller, T. S.; MacPherson, J. V.; Unwin, P. R. Comparison and Reappraisal of Carbon Electrodes for the Voltammetric Detection of Dopamine. *Anal. Chem.* **2013**, *85*, 11755−11764.
(56) Desimoni, E.; Casella, G. I.; Morone, A.; Salvi, A. M. XPS Determination of Oxygen-containing Functional Groups on Carbon-fibre Surfaces and the Cleaning of These Surfaces. *Surf. Interface Anal.* **1990**, *15*, 627−634.
(57) Sternitzke, K. D.; McCreery, R. L. Laser Microfabrication and Activation of Graphite and Glassy Carbon Electrodes. *Anal. Chem.* **1990**, *62*, 1339−1344.
(58) Poon, M.; Mccreery, R. L. In Situ Laser Activation of Glassy Carbon Electrodes. *Anal. Chem.* **1986**, *58*, 2745−2750.
(59) Patel, A. N.; Collignon, M. G.; O'Connell, M. A.; Hung, W. O. Y.; McKelvey, K.; MacPherson, J. V.; Unwin, P. R. A New View of Electrochemistry at Highly Oriented Pyrolytic Graphite. *J. Am. Chem. Soc.* **2012**, *134*, 20117−20130.
(60) Yuan, Y.; Lee, T. R. Contact Angle and Wetting Properties. In *Surface Science Techniques*; Bracco, G., Holst, B., Eds.; Springer Series in Surface Sciences; Springer: Berlin, 2013; Vol *51*.
(61) Park, J.; Han, H. S.; Kim, Y. C.; Ahn, J. P.; Ok, M. R.; Lee, K. E.; Lee, J. W.; Cha, P. R.; Seok, H. K.; Jeon, H. Direct and Accurate Measurement of Size Dependent Wetting Behaviors for Sessile Water Droplets. *Sci. Rep.* **2016**, *5*, 18150.
(62) Kozbial, A.; Li, Z.; Sun, J.; Gong, X.; Zhou, F.; Wang, Y.; Xu, H.; Liu, H.; Li, L. ScienceDirect Understanding the Intrinsic Water Wettability of Graphite. *Carbon* **2014**, *74*, 218−225.
(63) Hong, G.; Han, Y.; Schutzius, T. M.; Wang, Y.; Pan, Y.; Hu, M.; Jie, J.; Sharma, C. S.; Müller, U.; Poulikakos, D. On the Mechanism of Hydrophilicity of Graphene. *Nano Lett.* **2016**, *16*, 4447−4453.
(64) Kozbial, A.; Trouba, C.; Liu, H.; Li, L. Characterization of the Intrinsic Water Wettability of Graphite Using Contact Angle Measurements: Effect of Defects on Static and Dynamic Contact Angles. *Langmuir* **2017**, *33*, 959−967.
(65) Vashist, S. K.; Zheng, D.; Al-Rubeaan, K.; Luong, J. H. T.; Sheu, F. S. Advances in Carbon Nanotube Based Electrochemical Sensors for Bioanalytical Applications. *Biotechnol. Adv.* **2011**, *29*, 169−188.
(66) Papakonstantinou, P.; Kern, R.; Robinson, L.; Murphy, H.; Irvine, J.; McAdams, E.; McLaughlin, J.; McNally, T. Fundamental Electrochemical Properties of Carbon Nanotube Electrodes. *Fullerenes, Nanotubes, Carbon Nanostruct.* **2005**, *13*, 91−108.
(67) Li, X.; Forouzandeh, F.; Kakanat, A. J.; Feng, F.; Banham, D. W. H.; Ye, S.; Kwok, D. Y.; Birss, V. Surface Characteristics of Microporous and Mesoporous Carbons Functionalized with Pentafluorophenyl Groups. *ACS Appl. Mater. Interfaces* **2018**, *10*, 2130−2142.
(68) Coates, J. Interpretation of Infrared Spectra, A Practical Approach. In *Encyclopedia of Analytical Chemistry: Applications, Theory and Instrumentation*; Myers, R. A., Ed.; John Wiley & Sons: Chichester, UK, 2000; pp 10815−10837.
(69) Smidt, E.; Lechner, P.; Schwanninger, M.; Haberhauer, G.; Gerzabek, M. H. Characterization of Waste Organic Matter by FT-IR Spectroscopy: Application in Waste Science. *Appl. Spectrosc.* **2002**, *56*, 1170−1175.
(70) Mücksch, C.; Rösch, C.; Müller-Renno, C.; Ziegler, C.; Urbassek, H. M. Consequences of Hydrocarbon Contamination for Wettability and Protein Adsorption on Graphite Surfaces. *J. Phys. Chem. C* **2015**, *119*, 12496−12501.
(71) Taherian, F.; Marcon, V.; Van Der Vegt, N. F. A.; Leroy, F. What Is the Contact Angle of Water on Graphene? *Langmuir* **2013**, *29*, 1457−1465.
(72) Li, Z.; Wang, Y.; Kozbial, A.; Shenoy, G.; Zhou, F.; McGinley, R.; Ireland, P.; Morganstein, B.; Kunkel, A.; Surwade, S. P.; Li, L.; Liu, H. Effect of Airborne Contaminants on the Wettability of Supported Graphene and Graphite. *Nat. Mater.* **2013**, *12*, 925−931.
(73) Wei, Y.; Jia, C. Q. Intrinsic Wettability of Graphitic Carbon. *Carbon* **2015**, *87* (C), 10−17.
(74) Liu, H.; Li, L. Graphitic Materials: Intrinsic Hydrophilicity and Its Implications. *Extreme Mechanics Letts* **2017**, *14*, 44−50.
(75) Ashraf, A.; Wu, Y.; Wang, M. C.; Yong, K.; Sun, T.; Jing, Y.; Haasch, R. T.; Aluru, N. R.; Nam, S. Doping-Induced Tunable Wettability and Adhesion of Graphene. *Nano Lett.* **2016**, *16*, 4708−4712.

DOI: 10.1021/acsanm.8b01887
ACS Appl. Nano Mater. 2019, 2, 228−240

(76) Tian, T.; Lin, S.; Li, S.; Zhao, L.; Santos, E. J. G.; Shih, C. J. Doping-Driven Wettability of Two-Dimensional Materials: A Multiscale Theory. *Langmuir* **2017**, *33*, 12827−12837.
(77) Sun, B.; Skyllas-Kazacos, M. Modification of Graphite Electrode Materials for Vanadium Redox Flow Battery Application—I. Thermal Treatment. *Electrochim. Acta* **1992**, *37*, 1253−1260.
(78) Smith, R. E. G.; Davies, T. J.; Baynes, N. D. B.; Nichols, R. J. The Electrochemical Characterisation of Graphite Felts. *J. Electroanal. Chem.* **2015**, *747*, 29−38.
(79) Pimenta, M. A.; Dresselhaus, G.; Dresselhaus, M. S.; Cançado, L. G.; Jorio, A.; Saito, R. Studying Disorder in Graphite-Based Systems by Raman Spectroscopy. *Phys. Chem. Chem. Phys.* **2007**, *9*, 1276−1291.
(80) Chieu, T. C.; Dresselhaus, M. S.; Endo, M. Raman Studies of Benzene-Derived Graphite Fibers. *Phys. Rev. B: Condens. Matter Mater. Phys.* **1982**, *26*, 5867−5877.
(81) Stobinski, L.; Lesiak, B.; Kövér, L.; Tóth, J.; Biniak, S.; Trykowski, G.; Judek, J. Multiwall Carbon Nanotubes Purification and Oxidation by Nitric Acid Studied by the FTIR and Electron Spectroscopy Methods. *J. Alloys Compd.* **2010**, *501*, 77−84.
(82) Wu, J.-B.; Lin, M.-L.; Cong, X.; Liu, H.-N.; Tan, P.-H. Raman Spectroscopy of Graphene-Based Materials and Its Applications in Related Devices. *Chem. Soc. Rev.* **2018**, *47*, 1822−1873.
(83) Cancado, L.; Takai, K.; Enoki, T. General Equation for the Determination of the Crystallite Size La of Nanographite by Raman Spectroscopy. *Appl. Phys. Lett.* **2006**, *88*, 163106.
(84) Vázquez-Santos, M. B.; Geissler, E.; László, K.; Rouzaud, J. N.; Martínez-Alonso, A.; Tascón, J. M. D. Comparative XRD, Raman, and TEM Study on Graphitization of PBO-Derived Carbon Fibers. *J. Phys. Chem. C* **2012**, *116*, 257−268.
(85) Xie, X.; Zhou, Y.; Bi, H.; Yin, K.; Wan, S.; Sun, L. Large-Range Control of the Microstructures and Properties of Three-Dimensional Porous Graphene. *Sci. Rep.* **2013**, *3*, 2117.
(86) Kuang, J.; Liu, L.; Gao, Y.; Zhou, D.; Chen, Z.; Han, B.; Zhang, Z. A Hierarchically Structured Graphene Foam and Its Potential as a Large-Scale Strain-Gauge Sensor. *Nanoscale* **2013**, *5*, 12171−12177.
(87) Mao, X.; Simeon, F.; Rutledge, G. C.; Hatton, T. A. Electrospun Carbon Nanofiber Webs with Controlled Density of States for Sensor Applications. *Adv. Mater.* **2013**, *25*, 1309−1314.
(88) Sun, B.; Skyllas-Kazacos, M. Chemical Modification of Graphite Electrode Materials for Vanadium Redox Flow Battery Application-Part II. Acid Treatments. *Electrochim. Acta* **1992**, *37*, 2459−2465.
(89) Ding, C.; Zhang, H.; Li, X.; Liu, T.; Xing, F. Vanadium Flow Battery for Energy Storage: Prospects and Challenges. *J. Phys. Chem. Lett.* **2013**, *4*, 1281−1294.
(90) Mazúr, P.; Mrlík, J.; Beneš, J.; Pocedič, J.; Vrána, J.; Dundálek, J.; Kosek, J. Performance Evaluation of Thermally Treated Graphite Felt Electrodes for Vanadium Redox Flow Battery and Their Four-Point Single Cell Characterization. *J. Power Sources* **2018**, *380*, 105−114.
(91) Yamaguchi, H.; Ogawa, S.; Watanabe, D.; Hozumi, H.; Gao, Y.; Eda, G.; Mattevi, C.; Fujita, T.; Yoshigoe, A.; Ishizuka, S.; Adamska, L.; Yamada, T.; Dattelbaum, A. M.; Gupta, G.; Doorn, S. K.; Velizhanin, K. A.; Teraoka, Y.; Chen, M.; Htoon, H.; Chhowalla, M.; Mohite, A. D.; Takakuwa, Y. Valence-Band Electronic Structure Evolution of Graphene Oxide upon Thermal Annealing for Optoelectronics. *Phys. Status Solidi A* **2016**, *213*, 2380−2386.
(92) McFeely, F. R.; Kowalczyk, S. P.; Ley, L.; Cavell, R. G.; Pollak, R. A.; Shirley, D. A. X-Ray Photoemission Studies of Diamond, Graphite, and Glassy Carbon Valence Bands. *Phys. Rev. B* **1974**, *9*, 5268−5278.
(93) Jeong, H. K.; Hong, L.; Zhang, X.; Vega, E.; Dowben, P. A. Evidence of Band Bending and Surface Fermi Level Pinning in Graphite Oxide. *Carbon* **2013**, *57*, 227−231.
(94) Ganguly, A.; Sharma, S.; Papakonstantinou, P.; Hamilton, J. Probing the Thermal Deoxygenation of Graphene Oxide Using High-Resolution in Situ X-Ray-Based Spectroscopies. *J. Phys. Chem. C* **2011**, *115*, 17009−17019.
(95) Verkhovtsev, A. V.; Schramm, S.; Solov'Yov, A. V. Molecular Dynamics Study of the Stability of a Carbon Nanotube atop a Catalytic Nanoparticle. *Eur. Phys. J. D* **2014**, *68*, 246.
(96) Solov'yov, I. A.; Mathew, M.; Solov'Yov, A. V.; Greiner, W. Liquid Surface Model for Carbon Nanotube Energetics. *Phys. Rev. E - Stat. Nonlinear, Soft Matter Phys.* **2008**, *78*, 051601.
(97) Norris, D.; Bawendi, M. Measurement and Assignment of the Size-Dependent Optical Spectrum in CdSe Quantum Dots. *Phys. Rev. B: Condens. Matter Mater. Phys.* **1996**, *53*, 16338−16346.
(98) Joachim, C.; Gimzewski, J. K.; Aviram, A. Electronics Using Hybrid-Molecular and Mono-Molecular Devices. *Nature* **2000**, *408*, 541−548.
(99) Essler, F. H. L.; Frahm, H.; Göhmann, F.; Klümper, A.; Korepin, V. E. *The One-Dimensional Hubbard Model*; Cambridge University Press; 2005.
(100) Guerret-Piecourt, C.; Bec, S.; Treheux, D. Electrical Charges and Tribology of Insulating Materials. *C. R. Acad. Sci., Ser. IV: Phys., Astrophys.* **2001**, *2*, 761−774.
(101) Borodinov, N.; Ievlev, A. V.; Carrillo, J.; Calamari, A.; Mamak, M.; Mulcahy, J.; Sumpter, B. G.; Ovchinnikova, O. S.; Maksymovych, P. *Probing Static Discharge of Polymer Surfaces with Nanoscale Resolution*; **2018**; arXiv:1806.05169v1 [physics.app-ph].
(102) Hod, O. Graphite and Hexagonal Boron-Nitride Have the Same Interlayer Distance. Why? *J. Chem. Theory Comput.* **2012**, *8*, 1360−1369.
(103) Poenitzsch, V. Z.; Winters, D. C.; Xie, H.; Dieckmann, G. R.; Dalton, A. B.; Musselman, I. H. Effect of Electron-Donating and Electron-Withdrawing Groups on Peptide/Single-Walled Carbon Nanotube Interactions. *J. Am. Chem. Soc.* **2007**, *129*, 14724−14732.
(104) Kamaras, K.; Itkis, M. E.; Hu, H.; Zhao, B.; Haddon, R. C. Covalent Bond Formation to a Carbon Nanotube Metal. *Science* **2003**, *301*, 1501.
(105) Geim, A. K.; Novoselov, K. S. The Rise of Graphene. *Nat. Mater.* **2007**, *6*, 183−191.

DOI: 10.1021/acsanm.8b01887
ACS Appl. Nano Mater. 2019, 2, 228−240